NANO LETTERS

pubs.acs.org/NanoLett Letter

Exsolution-Driven Surface Transformation in the Host Oxide

Jiayue Wang, Abinash Kumar, Jenna L. Wardini, Zhan Zhang, Hua Zhou, Ethan J. Crumlin, Jerzy T. Sadowski, Kevin B. Woller, William J. Bowman, James M. LeBeau, and Bilge Yildiz*

Cite This: *Nano Lett.* 2022, 22, 5401−5408 Read Online

ACCESS | Metrics & More | Article Recommendations | Supporting Information

ABSTRACT: Exsolution synthesizes self-assembled metal nanoparticle catalysts via phase precipitation. An overlooked aspect in this method thus far is how exsolution affects the host oxide surface chemistry and structure. Such information is critical as the oxide itself can also contribute to the overall catalytic activity. Combining X-ray and electron probes, we investigated the surface transformation of thin-film $SrTi_{0.65}Fe_{0.35}O_3$ during Fe^0 exsolution. We found that exsolution generates a highly Fe-deficient near-surface layer of about 2 nm thick. Moreover, the originally single-crystalline oxide near-surface region became partially polycrystalline after exsolution. Such drastic transformations at the surface of the oxide are important because the exsolution-induced nonstoichiometry and grain boundaries can alter the oxide ion transport and oxygen exchange kinetics and, hence, the catalytic activity toward water splitting or hydrogen oxidation reactions. These findings highlight the need to consider the exsolved oxide surface, in addition to the metal nanoparticles, in designing the exsolved nanocatalysts.

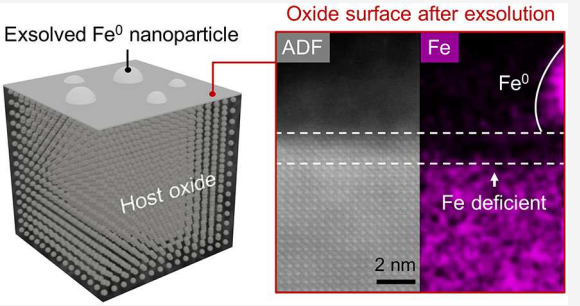

KEYWORDS: *exsolution, self-assembly, perovskite oxides, surface transformation, nanoparticles*

In renewable energy technologies today, a central theme is to design nanostructured catalysts at the solid/gas and solid/liquid interfaces toward desired reactions.[1,2] Exsolution[2−4] (Figure 1a) is a promising approach to generate self-assembled metal nanoparticle catalysts via phase precipitation, which often occurs when the host oxide is chemically[5,6] or electrochemically[7,8] reduced. Unlike the deposited or infiltrated nanoparticles, the exsolved nanoparticles are anchored in the host oxide,[9−11] which makes them more resistant against particle agglomeration and carbon poisoning (i.e., coking).[9,11] As a result, the exsolved nanoparticles often exhibit outstanding catalytic stability[6,12] under operating conditions and have been applied to a broad range of applications such as three-way catalysts,[6] solid oxide fuel/electrolysis cells,[13,14] and ceramic membrane reactors.[15]

Extensive efforts have been made in the past decade to optimize the composition,[16] size,[17,18] and density[18] of the exsolved nanoparticles to efficiently catalyze various reactions of importance to energy conversion. However, an equally important component in the exsolved system—the host oxide surface after exsolution—has received little attention. Since the host oxides used in exsolution are often mixed ionic and electronic conductors (MIEC),[19] they can be inherently active in (electro)catalysis if the ideal ionic and electronic structure is present in the oxide. Consequently, the active reaction zones on the exsolved metal−oxides are not necessarily constrained to the metal nanoparticles but can extend to the oxide surfaces.[20] For example, Roy et al. found that the catalytic activity of the exsolved calcium cobalt oxide increased after etching away the surface nanoparticles.[21] This interesting observation indicates that the remaining host oxides after exsolution may be more catalytically active than the exsolved nanoparticles, although we must note that the etching process may introduce potential artifacts to the oxide chemistry. The need to investigate the exsolved host oxide is further seen from recent studies where reduced or invariable performance was observed after exsolution.[22−24] For example, while Pd nanoparticles are excellent catalysts for CO oxidation reactions,[25] Singh et al. found that the catalytic activity of Pd-doped $BaCeO_{3-\delta}$ for CO oxidation decreases after Pd exsolution.[22] These results may seem counterintuitive and clearly demonstrate that one should carefully consider not only the exsolved nanoparticles but also what happens to the host oxide during exsolution.

As exsolution is a partial decomposition process, it can change the chemistry,[5,18] morphology,[26] and microstructure[8,10] of the host oxide surface, while precipitating the metal nanoparticles. It is well-known that surface grain boundaries,[27,28] lattice defects,[29,30] atomic structures,[31] and compositions[32,33] can greatly affect the kinetics of oxygen exchange at

Received: April 9, 2022
Revised: June 2, 2022
Published: June 30, 2022

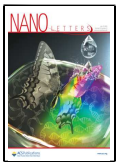

https://doi.org/10.1021/acs.nanolett.2c01439
Nano Lett. 2022, 22, 5401−5408

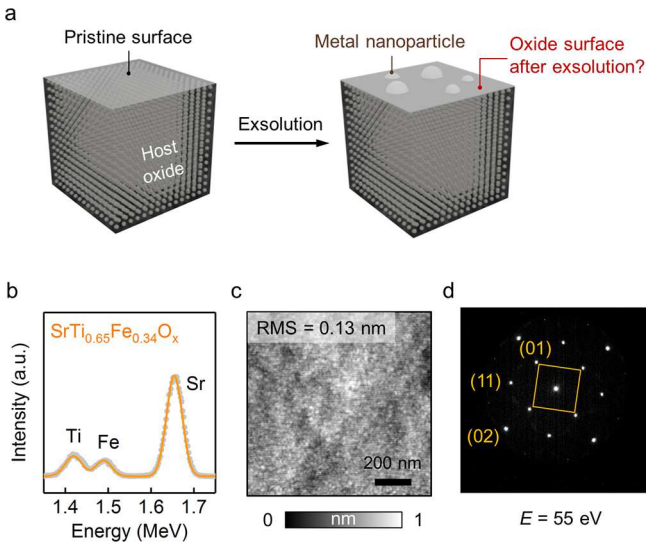

Figure 1. Paper theme and sample description. (a) Sketch of the exsolution process, which shows that exsolution not only generates supported metal nanoparticles but also transforms the host oxide surface. The aim of this work is to resolve how the surface chemistry and structure of the host oxide change upon exsolution. (b–d) Characterizations of the as-prepared STF film: (b) RBS data and the corresponding fitting results revealing the film composition. (c) AFM image showing the smooth surface morphology. (d) LEED pattern showing the p(1 × 1) (001) surface structure, where the 4-fold symmetry is highlighted by the solid square. From parts (b)–(d), we confirm that the as-prepared epitaxial STF film has well-defined composition, morphology, and structure.

the surface and oxide ion transport within the material. Therefore, any chemical and structural transformations on/in the oxide should also be considered in interpreting the changes in catalytic activity upon exsolution. To date, the detailed mechanism regarding the exsolution-induced surface transformation in the host oxide remains an open question. For example, a common assumption in today's literature is that exsolution is associated with the surface enrichment/segregation of the to-be-exsolved cations.[34−39] However, whether the hypothesized cation-enriched surface layer exists on the exsolved host oxide has never been experimentally validated.

Here, we aim to bridge this knowledge gap by investigating the surface transformation of perovskite $SrTi_{0.65}Fe_{0.35}O_3$ (STF) thin films during metallic iron (Fe^0) exsolution. We chose STF as a model system due to its technological relevance to the solid oxide fuel/electrolysis cells.[16,40] Combining grazing incidence synchrotron X-ray diffraction, *in situ* X-ray photoelectron spectroscopy, and scanning transmission electron microscopy, we systematically characterized the exsolution-induced chemical and structural evolution at the STF surface. As a result, we demonstrate unambiguously that the top ∼2 nm of the STF surface become highly Fe-deficient after Fe^0 exsolution. Moreover, the as-prepared single-crystalline STF near-surface region became partially polycrystalline after exsolution. The drastic exsolution-driven chemical and structural transformation at the oxide surface has implications for the surface reaction kinetics such as water splitting, hydrogen oxidation, and oxygen exchange reactions, and calls for attention of the field to consider these changes in the interpretation of catalytic activity upon metal nanoparticle exsolution.

Epitaxial STF films were grown on the (001)-oriented $SrTiO_3$ (STO) and Nb-doped $SrTiO_3$ single crystal substrates using pulsed laser deposition (see Methods). To verify the chemical composition of the STF film, we conducted Rutherford backscattering spectrometry (RBS), and the result is shown in Figure 1b. The quantified film composition is $SrTi_{0.65}Fe_{0.34}O_x$, which agrees with its nominal value (i.e., $SrTi_{0.65}Fe_{0.35}O_{3-\delta}$). We then conducted atomic force microscopy (AFM) and low-energy electron diffraction (LEED) measurements to probe the surface morphology and structure of the as-prepared STF films. As a result, AFM imaging (Figure 1c) shows that the as-prepared STF has a smooth surface, with root-mean-square (RMS) roughness of ∼0.1 nm. Meanwhile, the LEED pattern (Figure 1d) shows a characteristic p(1 × 1) perovskite (001) surface structure with a 4-fold symmetry. The (001) orientation of the STF film is also confirmed via out-of-plane $\theta-2\theta$ X-ray diffraction measurements (Figure S1). Based on these characterizations, we confirm that the as-prepared STF films have well-defined surface structure, morphology and composition, which can serve as an ideal model system to investigate the exsolution-driven surface transformation.

We first conducted *in situ* near ambient pressure X-ray photoelectron spectroscopy (NAP-XPS) measurements to track the surface chemistry evolution of the STF film during Fe^0 exsolution. In the measurement, we heated the STF film up to 600 °C in 75 mTorr H_2 and collected core-level spectra at different temperatures (see Methods). As shown in Figure 2a, the Ti 2*p* and Sr 3*d* spectra profile remained relatively stable during the entire course of the measurement. On the other hand, there is a significant evolution in the Fe 3*p* spectra: Metallic iron species[18,41] (Fe^0) started to appear at ∼52.5 eV in the Fe 3*p* spectra when the STF film was heated to 500 °C in H_2, which marks the onset of Fe^0 exsolution in STF.

Using the fitting methods described in Figures S2–S4, we deconvoluted the NAP-XPS spectra to quantify the surface chemistry evolution. As shown in Figure 2a, $Ti_{lattice}$ in Ti 2*p* denotes the lattice Ti^{4+} component in STF. Meanwhile, $Sr_{lattice}$ and Sr_{surf} represent the lattice Sr^{2+} and the segregated surface Sr species, respectively. Such a fitting model for Sr has been commonly used in the literature to account for the potential Sr segregation[42−44] on perovskites surfaces. Finally, for the Fe 3*p* spectra, we fit the spectra with lattice Fe^{2+}/Fe^{3+} ($Fe_{lattice}$[18]), exsolved metal Fe^0, and a satellite component from Sr and Ti at ∼50 eV. With the deconvolutions described above, we plot the surface concentrations of Fe^0 and Sr_{surf} in Figure 2b as a function of the annealing temperature. As illustrated, the surface Fe^0 concentration increased with the annealing temperature, consistent with metal precipitation. The Sr_{surf} concentration remained largely stable, confirming negligible Sr segregation[44] under the current experimental conditions. To quantify the lattice Fe concentrations on the STF surface, we plot the $Fe_{lattice}$ intensity normalized with Ti and Sr in Figure 2c. Such a normalization procedure is necessary to reveal the surface compositional evolution, as variations in both temperature[45] and surface morphology/roughness[46] can change the NAP-XPS intensities. As a result, we found that both the Ti- and Sr-normalized $Fe_{lattice}$ intensities decrease by as much as ∼63% after exsolution. These observations clearly indicate that the STF surface became Fe-deficient after Fe^0 exsolution.

We then characterized the surface morphology of the STF film after the NAP-XPS measurement using *ex-situ* AFM imaging (Figure 3a). In contrast to the originally smooth surface morphology (Figure 1c), nanoparticles can now be

https://doi.org/10.1021/acs.nanolett.2c01439
Nano Lett. 2022, 22, 5401−5408

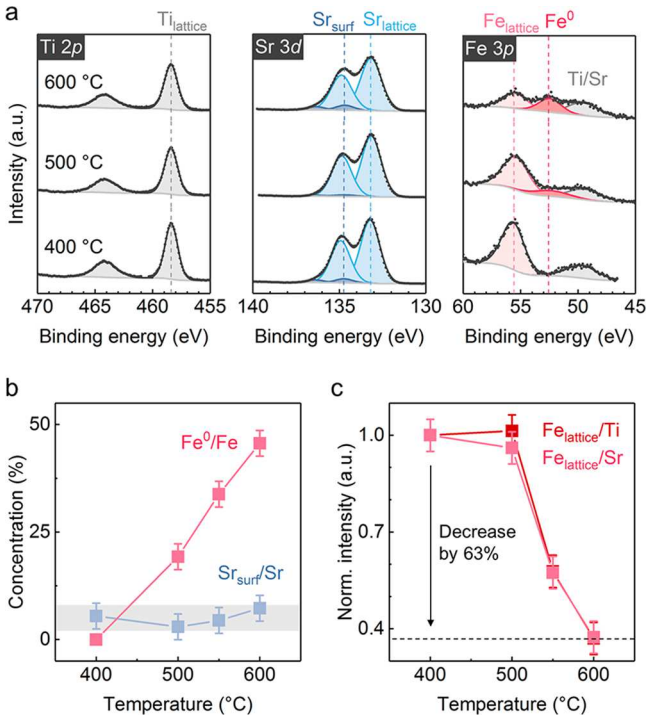

Figure 2. Exsolution-induced surface Fe depletion revealed by NAP-XPS. (a) *In situ* NAP-XPS spectra of the STF film while being heated in 75 mTorr H_2. All the spectra are collected at a photon energy of 665 eV. (b) Evolution of the metallic iron (Fe^0) and segregated Sr (Sr_{surf}) concentrations during the experiment. The surface concentration of Fe^0 increased with temperature, while the Sr_{surf} concentration remained stable. (c) Evolution of the lattice Fe intensity during exsolution, normalized to the total Ti and Sr intensities. Note that, for both types of normalizations, the normalized $Fe_{lattice}$ intensities decreased significantly after the onset of Fe^0 exsolution. This observation indicates that the STF surface became Fe-deficient after Fe^0 exsolution.

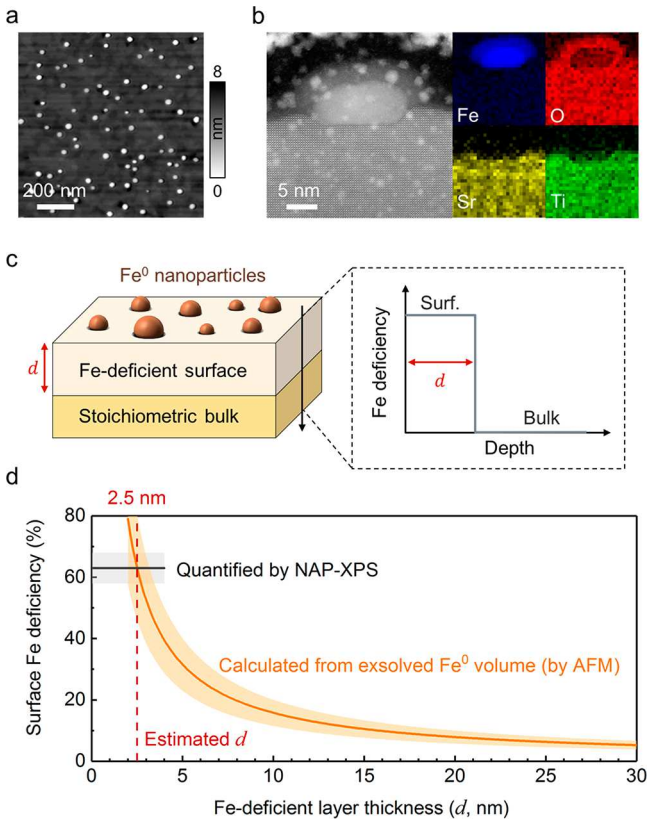

Figure 3. Estimation of the Fe-deficient layer thickness in the exsolved STF film. (a) AFM image of the STF film after the NAP-XPS measurement (Figure 2). Note that the exsolved Fe^0 particles are present on the surface. (b) High-angle annular dark-field image (HAADF) and the corresponding EELS-based chemical map of an exsolved Fe nanoparticle. The tiny particles in the HAADF image are Pt clusters introduced during the TEM sample preparation and the Sr intensity modulation in the EELS map is due to a sampling artifact. (c) Bilayer model for estimating the Fe-deficient layer thickness (denoted as d) at the surface of the exsolved STF film. The model assumes that exsolution generates a surface layer with a uniform Fe deficiency. (d) Calculated surface Fe deficiency (yellow solid line) in the exsolved STF as a function of the Fe-deficient layer thickness (i.e., d). The NAP-XPS quantified surface Fe deficiency is shown by the gray line. Based on the intersection of the yellow and gray lines, we estimate the Fe-deficient layer thickness in the exsolved STF film to be ~2.5 nm (indicated by the dashed red line). The shaded bands represent the uncertainties in the AFM and NAP-XPS quantifications.

clearly observed on the exsolved STF surface. With the aid of electron energy loss spectroscopy (EELS), we confirmed these nanoparticles are iron (Figure 3b). Note that the exsolved Fe^0 nanoparticle in Figure 3b is encapsulated by a thin layer of iron oxide, which is due to the passivation by oxygen in air when the sample was taken out of the exsolution experiment.[18,41] From 10 representative AFM images, we quantified the area-specific volumes of the surface nanoparticles to be 0.11 ± 0.03 nm^3/nm^2. Other particle statistics (including particle size, density, and surface coverage) are summarized in Figure S5. We note that the surface coverage of the exsolved nanoparticles is rather low (~4%), which implies that most NAP-XPS signals in Figure 2 are collected from the oxide surface regions that are not covered by the nanoparticles. This observation provides additional support that the observed surface Fe depletion in the oxide lattice is real, and not an artifact in the XPS data collection.

Based on the volume of the exsolved Fe^0 nanoparticles, we further estimate the thickness of the Fe-deficient layer in the exsolved STF film using a bilayer model (Figure 3c). In this model, the exsolved STF film consists of a Fe-deficient surface layer with thickness d, and a stoichiometric bulk without any Fe deficiency (i.e., $SrTi_{0.65}Fe_{0.35}O_{3-\delta}$). We assume that the surface layer in the exsolved STF film has a uniform Fe deficiency and that all the Fe atoms in exsolved nanoparticles are drawn out from this Fe-deficient surface layer. As a result, for any given Fe-deficient layer thickness (i.e., d), we can calculate the corresponding Fe deficiency in that layer based on the mass conservation of Fe. In the calculation, we consider the Fe^0 nanoparticles to be α-Fe (space group $Im\bar{3}m$, lattice parameter 2.87 Å), while the exsolved STF surface has a cubic perovskite structure (space group $Pm\bar{3}m$, lattice parameter 3.90 Å). These structural assignments are based on previous studies on the exsolved Fe nanoparticles[41,47] as well as the grazing incident X-ray diffraction characterizations on the exsolved STF film (to be discussed in Figure 5). We are aware that the uniform bilayer model described above can be an over-simplification of the reality, where compositional gradients can be developed near the surface after exsolution. Nevertheless, we adopt this model in this study as a first-order approximation of the thickness of the surface Fe-deficient layer.

The obtained relationship between the average Fe deficiency and the thickness d of the Fe-deficient surface layer is shown

https://doi.org/10.1021/acs.nanolett.2c01439
Nano Lett. 2022, 22, 5401−5408

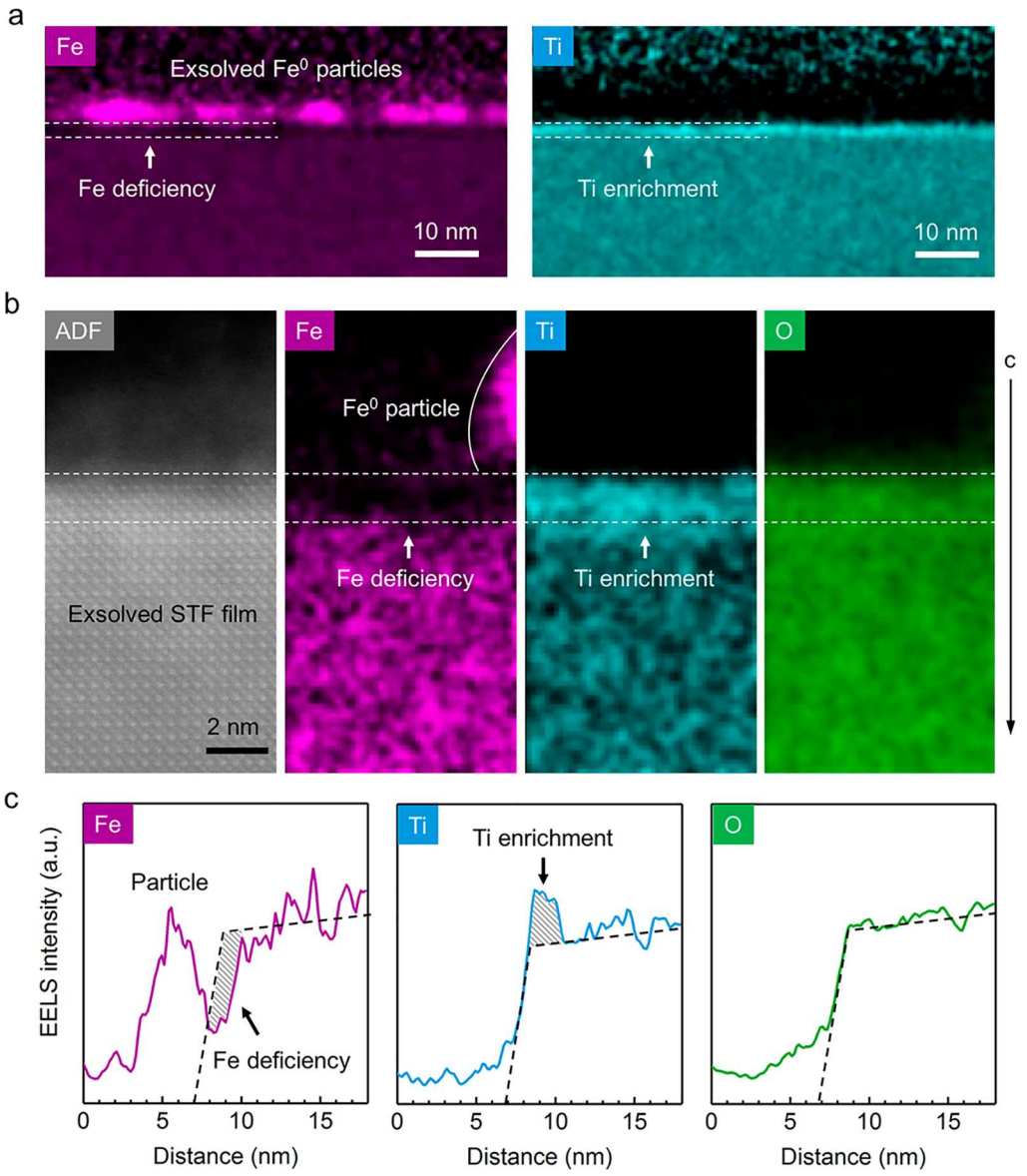

Figure 4. Nanoscale chemical analysis of the exsolved STF surface. (a) EDX chemical maps, where the color intensities represent the atomic concentrations. (b) Annular dark-field (ADF) image, together with the corresponding EELS chemical maps. The colors in the EELS maps represent absolute intensities. (c) Averaged EELS intensity profiles of the Fe, Ti, and O maps, with the profiling direction highlighted by the arrow in plot (b). The dashed lines in plot (c) represent the simplified profile of the O intensity, which serve as the guide to the eyes. The shaded regions in the Fe and Ti maps clearly demonstrate that the exsolved STF surface is depleted in Fe while enriched in Ti. The sample was exsolved in vacuum at 800 °C.

with the solid yellow line in Figure 3d. As expected, the average surface Fe deficiency is inversely proportional to the surface layer thickness: Given the fixed amount of exsolved Fe^0, the wider the Fe-deficient layer, the smaller the averaged Fe deficiency in the layer will be. Using this curve, we can thus estimate the surface Fe-deficient layer from the NAP-XPS quantified surface Fe deficiency (Figure 2c). As indicated by the red dashed line in Figure 3d, the estimated surface Fe-deficient layer thickness is 2.5 nm. Note that this value should be perceived with caution as there are several simplified assumptions behind it. For example, in addition to the bilayer model itself, we have also neglected the embedded volume of the exsolved nanoparticles and have assumed that surface nanoparticles are completely Fe^0 (without iron oxide surface layer). Therefore, the estimated 2.5 nm should only be treated as a semiquantitative indication that the surface Fe-deficient layer is very narrow (on the order of a few nanometers).

To confirm the near-surface Fe depletion, we performed nanoscale chemical mapping of the as-prepared and exsolved STF films using energy dispersive X-ray spectroscopy (EDX) and EELS. In particular, we examined two STF films that were exsolved at different conditions. The first sample was exsolved during the NAP-XPS measurement (Figure 2), while the second one was exsolved by 800 °C vacuum annealing (see Methods). As will be elaborated below, we observed ~2 nm near-surface Fe depletion for both types of the exsolved samples, suggesting that the exsolution-induced surface Fe depletion near the very surface is a generalized phenomenon, regardless of the exsolution condition.

As shown in Figure S6, the as-prepared STF has a homogeneous chemistry across the entire sample. However,

https://doi.org/10.1021/acs.nanolett.2c01439
Nano Lett. 2022, 22, 5401−5408

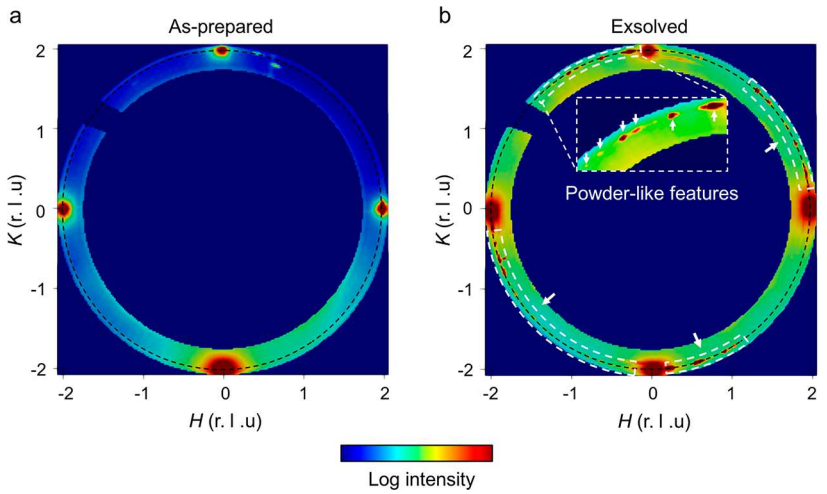

Figure 5. Structural evolution of the STF film during exsolution. Grazing incident X-ray reciprocal space mapping in the vicinity of the STF/STO (200) Bragg peaks (HK slices at L = 0.04) for the (a) as-prepared and (b) exsolved STF film. Note that, for the as-prepared STF film, a 4-fold symmetry can be observed without any other component present, which confirms the single-crystalline nature of the as-prepared STF film. Nevertheless, after exsolution, powder-like features (highlighted by the dashed boxes and arrows) started to appear. This clearly indicates that the near-surface region of the STF film evolved structurally during exsolution and became partially polycrystalline. The dashed circles represent the amplitude of the momentum transfer, |Q|, of the STF (200) reflection. The sample was exsolved in vacuum at 800 °C.

significant chemical inhomogeneities develop at the surface of the exsolved (vacuum annealed) STF (Figure 4a,b). In particular, a clear intensity drop in the Fe maps (highlighted by the dashed lines) can be observed on the exsolved STF surface right beneath the exsolved Fe^0 nanoparticles. Meanwhile, a bright intensity band appears at the same location in the Ti maps. These observations indicate that the exsolved STF near-surface is depleted in Fe while enriched in Ti. Similar phenomena can be also observed on the STF films that were exsolved in the NAP-XPS conditions (Figure S7). To better visualize the Fe depletion and Ti enrichment at the exsolved STF surface, we plot the averaged EELS intensity profiles of the Fe, Ti, and O (calculated from Figure 4b) in Figure 4c. As EELS intensities depend on both the chemical concentration and the sample thickness, we use the O profile as our reference (indicated by the dashed line). As highlighted by the shaded regions in Figure 4c, the EELS intensities of Fe/Ti are considerably below/above that of the dashed lines within the top ∼2 nm of the surface, indicating significant surface Fe depletion and Ti enrichment. From the EELS maps, we estimated the surface Ti/Fe ratio to be 95:5, which is much higher than the nominal 65:35 value in the bulk. Due to Fe^0 exsolution, we also expect B-site deficiency in this layer; however, the exact surface stoichiometry was beyond our detection limit.

Based on the results described above, we can summarize some general features of the exsolution-induced surface chemical evolution. First, the STF surface became deficient in Fe but enriched in Ti after Fe^0 exsolution. Second, the exsolution-induced chemical transformation in the STF film is highly localized to the top ∼2 nm of the surface, while the subsurface ("bulk") chemistry remained uniform even after exsolution (see Figures S7−S8). It should be noted that for cases where exsolution takes place in the bulk,[48] the bulk chemistry of the host oxide can also evolve after bulk exsolution. For example, we have recently observed percolating Fe-deficient channels[41] (∼2 nm wide) and other Fe-deficient nanostructures[49] near the exsolved Fe^0 nanoparticles in the $La_{0.6}Sr_{0.4}FeO_3$ film after bulk exsolution. The similarities between these two cases (i.e., surface and bulk exsolutions) suggest that the formation of nanoscale regions that are depleted in the to-be-exsolved cations near the exsolved nanoparticles can be a general phenomenon in exsolution.

Finally, we collected the reciprocal space mapping (RSM) of the as-prepared and exsolved (vacuum annealed) STF films with grazing-incidence X-ray. As illustrated in Figure 5a, the RSM of the as-prepared STF surface shows a 4-fold symmetry for the STF/STO (200) diffractions. This observation confirms the single-crystalline nature of the as-prepared STF near-surface, which agrees well with the LEED measurement in Figure 1d. However, after exsolution, powder-like polycrystalline features (highlighted by the dashed boxes and arrows in Figure 5b) appear in the RSM. By examining the RSMs around other diffraction peaks and at an incidence below the critical angle (Figure S9), we confirm that the polycrystalline contribution is from the exsolved STF surface with random orientation (Figure S10). The formation of polycrystalline surface regions after exsolution can be also seen in the grazing incidence X-ray diffraction patterns (Figure S11). These observations clearly indicate that in addition to the compositional modulation described above, exsolution also transforms the microstructure of the near-surface region of the STF film. Note that from both RSM measurements (Figure 5 and S10) and ADF imaging (Figure 4b), we can tell that there is still some epitaxial portion of the surface zone remaining after exsolution, indicating that the top Fe-depleted layer is not fully polycrystalline. Therefore, our observations suggest the near-surface polycrystalline regions are spatially dispersed, making the exsolved STF partially polycrystalline near its surface. The structural changes on the exsolved STF surface could be caused by the substantial chemical contraction/expansion[50] of the surface lattice (Figure S12) and/or due to stress accumulation[26] near the metal−oxide interfaces.

In summary, by carrying out surface-sensitive characterizations using X-ray and electron probes, we revealed exsolution-driven chemical and structural transformation on the (001)-oriented STF thin film surfaces. We demonstrated unequivocally that the STF surface became highly Fe-deficient

https://doi.org/10.1021/acs.nanolett.2c01439
Nano Lett. 2022, 22, 5401−5408

(and Ti-enriched) after Fe^0 exsolution. In addition to the compositional change, the initially single-crystalline STF near-surface also become partially polycrystalline after exsolution. Intriguingly, we found that the exsolution-transformed surface layer in the exsolved STF film is quite thin, which is ~2 nm even after being exsolved at 800 °C. While our experiments were performed on single crystalline films, we believe similar chemical and structural transformations can also take place upon exsolution near the surface of the grains in a polycrystalline specimen. Grain boundaries on the MIEC surfaces are well-known to be preferential sites for oxygen exchange and oxygen diffusion.[27,28] In addition, the non-stoichiometry and defects (such as oxygen and cation vacancies) can also facilitate oxide ion transport in the lattice and oxygen exchange at the surface.[29,30] Therefore, the structure and density of the grain boundaries, as well as the nonstoichiometry on the exsolved oxide surface, can impact the oxygen exchange kinetics involved in high-temperature water splitting and hydrogen oxidation reactions. The drastic surface transformations that we have found during exsolution show that an isolated optimization of the exsolved metal nanoparticles alone for catalytic activity in a metal−oxide composite system is insufficient. Rather, the exsolved metal−oxide composite should be considered holistically in designing the exsolved nanocatalysts. We believe that dynamic tuning of the compositions and micro/nanostructures of the host oxide surface via exsolution offers an attractive avenue for designing the next-generation exsolved nanocatalysts.

■ ASSOCIATED CONTENT

Supporting Information

The Supporting Information is available free of charge at https://pubs.acs.org/doi/10.1021/acs.nanolett.2c01439.

Details of the experimental procedure, XRD and XPS analysis, statistics of nanoparticle morphology, grazing incidence X-ray diffraction patterns, and additional STEM characterizations (PDF)

■ AUTHOR INFORMATION

Corresponding Author

Bilge Yildiz − *Department of Nuclear Science and Engineering, Massachusetts Institute of Technology, Cambridge, Massachusetts 02139, United States; Department of Materials Science and Engineering, Massachusetts Institute of Technology, Cambridge, Massachusetts 02139, United States;* orcid.org/0000-0002-2688-5666; Email: byildiz@mit.edu

Authors

Jiayue Wang − *Department of Nuclear Science and Engineering, Massachusetts Institute of Technology, Cambridge, Massachusetts 02139, United States;* orcid.org/0000-0002-2027-3634

Abinash Kumar − *Department of Materials Science and Engineering, Massachusetts Institute of Technology, Cambridge, Massachusetts 02139, United States*

Jenna L. Wardini − *Department of Materials Science & Engineering, University of California, Irvine, California 92697, United States*

Zhan Zhang − *Advanced Photon Source, Argonne National Laboratory, Lemont, Illinois 60439, United States*

Hua Zhou − *Advanced Photon Source, Argonne National Laboratory, Lemont, Illinois 60439, United States;* orcid.org/0000-0001-9642-8674

Ethan J. Crumlin − *Advanced Light Source, Lawrence Berkeley National Laboratory, Berkeley, California 94720, United States;* orcid.org/0000-0003-3132-190X

Jerzy T. Sadowski − *Center for Functional Nanomaterials, Brookhaven National Laboratory, Upton, New York 11973, United States;* orcid.org/0000-0002-4365-7796

Kevin B. Woller − *Department of Nuclear Science and Engineering, Massachusetts Institute of Technology, Cambridge, Massachusetts 02139, United States*

William J. Bowman − *Department of Materials Science & Engineering, University of California, Irvine, California 92697, United States;* orcid.org/0000-0002-4346-1144

James M. LeBeau − *Department of Materials Science and Engineering, Massachusetts Institute of Technology, Cambridge, Massachusetts 02139, United States*

Complete contact information is available at: https://pubs.acs.org/10.1021/acs.nanolett.2c01439

Author Contributions

J.W. conceived the experiments, prepared the samples, and analyzed the data. J.W. and E.J.C. conducted the NAP-XPS measurements. J.W., Z.Z., and H.Z. conducted the RSM measurements. J.T.S. conducted the LEED measurement. K.B.W. conducted the RBS measurement. A.K. and J.L.W. performed the STEM characterization under the supervisions of J.M.L. and W.J.B., respectively. J.W. wrote the manuscript, and all authors contributed to its revision. B.Y. supervised the project.

Notes

The authors declare no competing financial interest.

■ ACKNOWLEDGMENTS

The authors thank the OxEon Corporation for supporting the work presented in this paper. This research used the synchrotron radiation facilities at the Center for Functional Nanomaterials and National Synchrotron Light Source II, U.S. Department of Energy (DOE) Office of Science User Facilities, operated for the DOE Office of Science by Brookhaven National Laboratory under Contract No. DE-SC0012704, and the Advanced Light Source, which is supported by the DOE Office of Basic Energy Sciences under Contract No. DE-AC02-05CH11231. This research also used the synchrotron radiation facilities at the Argonne, which was supported by the U.S. DOE under Contract No. DE-AC02-06CH11357. The authors acknowledge the facility support from the Center for Materials Science and Engineering at MIT (NSF under Award Number DMR-1419807) and the MIT.nano Characterization Facilities (Award DMR-2117609). J.L.W. and W.J.B. acknowledge funding under the award NSF CAREER DMR-2042638. The authors acknowledge the use of facilities and instrumentation at the UC Irvine Materials Research Institute (IMRI) supported in part by the National Science Foundation Materials Research Science and Engineering Center program through the UC Irvine Center for Complex and Active Materials (DMR-2011967). J.W. thanks Dr. Yang Yu for the assistance in the FIB preparation and Dr. Aubrey Penn for the assistance with STEM imaging. J.W. thanks Dr. Joseph G. Manion (@CG Figures) for the helpful discussion and assistance in the 3D visualization.

REFERENCES

(1) Mitchell, S.; Qin, R.; Zheng, N.; Pérez-Ramírez, J. Nanoscale engineering of catalytic materials for sustainable technologies. *Nat. Nanotechnol.* **2021**, *16*, 129−139.

(2) Irvine, J. T. S.; et al. Evolution of the electrochemical interface in high-temperature fuel cells and electrolysers. *Nature Energy* **2016**, *1*, 15014.

(3) Kousi, K.; Tang, C.; Metcalfe, I. S.; Neagu, D. Emergence and Future of Exsolved Materials. *Small* **2021**, *17*, 2006479.

(4) Kim, J. H.; et al. Nanoparticle Ex-solution for Supported Catalysts: Materials Design, Mechanism and Future Perspectives. *ACS Nano* **2021**, *15*, 81−110.

(5) Neagu, D.; Tsekouras, G.; Miller, D. N.; Ménard, H.; Irvine, J. T. S. In situ growth of nanoparticles through control of non-stoichiometry. *Nat. Chem.* **2013**, *5*, 916−923.

(6) Nishihata, Y.; et al. Self-regeneration of a Pd-perovskite catalyst for automotive emissions control. *Nature* **2002**, *418*, 164−167.

(7) Myung, J.-h.; Neagu, D.; Miller, D. N.; Irvine, J. T. S. Switching on electrocatalytic activity in solid oxide cells. *Nature* **2016**, *537*, 528−531.

(8) Opitz, A. K.; et al. Understanding electrochemical switchability of perovskite-type exsolution catalysts. *Nat. Commun.* **2020**, *11*, 4801.

(9) Neagu, D.; et al. Nano-socketed nickel particles with enhanced coking resistance grown in situ by redox exsolution. *Nat. Commun.* **2015**, *6*, 8120.

(10) Neagu, D.; et al. Situ Observation of Nanoparticle Exsolution from Perovskite Oxides: From Atomic Scale Mechanistic Insight to Nanostructure Tailoring. *ACS Nano* **2019**, *13*, 12996−13005.

(11) Yu, S.; et al. Metal Nanoparticle Exsolution on a Perovskite Stannate Support with High Electrical Conductivity. *Nano Lett.* **2020**, *20*, 3538−3544.

(12) Neagu, D.; et al. Demonstration of chemistry at a point through restructuring and catalytic activation at anchored nanoparticles. *Nat. Commun.* **2017**, *8*, 1855.

(13) Sun, Y.-F.; et al. New Opportunity for in Situ Exsolution of Metallic Nanoparticles on Perovskite Parent. *Nano Lett.* **2016**, *16*, 5303−5309.

(14) Tsekouras, G.; Neagu, D.; Irvine, J. T. S. Step-change in high temperature steam electrolysis performance of perovskite oxide cathodes with exsolution of B-site dopants. *Energy Environ. Sci.* **2013**, *6*, 256−266.

(15) Dimitrakopoulos, G.; Ghoniem, A. F.; Yildiz, B. In situ catalyst exsolution on perovskite oxides for the production of CO and synthesis gas in ceramic membrane reactors. *Sustainable Energy & Fuels* **2019**, *3*, 2347−2355.

(16) Zhu, T.; Troiani, H. E.; Mogni, L. V.; Han, M.; Barnett, S. A. Ni-Substituted Sr(Ti,Fe)O3 SOFC Anodes: Achieving High Performance via Metal Alloy Nanoparticle Exsolution. *Joule* **2018**, *2*, 478−496.

(17) Jo, Y.-R.; et al. Growth Kinetics of Individual Co Particles Exsolved on SrTi0.75Co0.25O3-δ Polycrystalline Perovskite Thin Films. *J. Am. Chem. Soc.* **2019**, *141*, 6690−6697.

(18) Wang, J.; et al. Tuning Point Defects by Elastic Strain Modulates Nanoparticle Exsolution on Perovskite Oxides. *Chem. Mater.* **2021**, *33*, 5021−5034.

(19) Chueh, W. C.; Haile, S. M. Electrochemistry of Mixed Oxygen Ion and Electron Conducting Electrodes in Solid Electrolyte Cells. *Annu. Rev. Chem. Biomol. Eng.* **2012**, *3*, 313−341.

(20) Chueh, W. C.; Hao, Y.; Jung, W.; Haile, S. M. High electrochemical activity of the oxide phase in model ceria−Pt and ceria−Ni composite anodes. *Nat. Mater.* **2012**, *11*, 155−161.

(21) Roy, K. S.; Subramaniam, C.; Panchakarla, L. S. Non-Stoichiometry Induced Exsolution of Metal Oxide Nanoparticles via Formation of Wavy Surfaces and their Enhanced Electrocatalytic Activity: Case of Misfit Calcium Cobalt Oxide. *ACS Appl. Mater. Interfaces* **2021**, *13*, 9897−9907.

(22) Singh, U. G.; et al. A Pd-doped perovskite catalyst, BaCe1−xPdxO3−δ, for CO oxidation. *J. Catal.* **2007**, *249*, 349−358.

(23) Opitz, A. K.; et al. Surface Chemistry of Perovskite-Type Electrodes During High Temperature CO2 Electrolysis Investigated by Operando Photoelectron Spectroscopy. *ACS Appl. Mater. Interfaces* **2017**, *9*, 35847−35860.

(24) Li, J.; et al. Hexagonal YFe1−xPdxO3−δ: Nonperovskite Host Compounds for Pd2+ and Their Catalytic Activity for CO Oxidation. *Chem. Mater.* **2008**, *20*, 6567−6576.

(25) Zhou, Y.; Wang, Z.; Liu, C. Perspective on CO oxidation over Pd-based catalysts. *Catalysis Science & Technology* **2015**, *5*, 69−81.

(26) Oh, T.-S.; et al. Evidence and Model for Strain-Driven Release of Metal Nanocatalysts from Perovskites during Exsolution. *J. Phys. Chem. Lett.* **2015**, *6*, 5106−5110.

(27) Navickas, E.; et al. Fast oxygen exchange and diffusion kinetics of grain boundaries in Sr-doped LaMnO3 thin films. *Phys. Chem. Chem. Phys.* **2015**, *17*, 7659−7669.

(28) Lee, W.; et al. Oxygen Surface Exchange at Grain Boundaries of Oxide Ion Conductors. *Adv. Funct. Mater.* **2012**, *22*, 965−971.

(29) Kuai, X.; et al. Boosting the Activity of BaCo0.4Fe0.4Zr0.1Y0.1O3−δ Perovskite for Oxygen Reduction Reactions at Low-to-Intermediate Temperatures through Tuning B-Site Cation Deficiency. *Adv. Energy Mater.* **2019**, *9*, 1902384.

(30) Su, C.; Wang, W.; Shao, Z. Cation-Deficient Perovskites for Clean Energy Conversion. *Accounts of Materials Research* **2021**, *2*, 477−488.

(31) Riva, M.; et al. Influence of surface atomic structure demonstrated on oxygen incorporation mechanism at a model perovskite oxide. *Nat. Commun.* **2018**, *9*, 3710.

(32) Baeumer, C.; et al. Tuning electrochemically driven surface transformation in atomically flat LaNiO3 thin films for enhanced water electrolysis. *Nat. Mater.* **2021**, *20*, 672−682.

(33) Stoerzinger, K. A.; et al. Influence of LaFeO3 Surface Termination on Water Reactivity. *J. Phys. Chem. Lett.* **2017**, *8*, 1038−1043.

(34) Kwon, O.; et al. Exsolution trends and co-segregation aspects of self-grown catalyst nanoparticles in perovskites. *Nat. Commun.* **2017**, *8*, 15967.

(35) Hamada, I.; Uozumi, A.; Morikawa, Y.; Yanase, A.; Katayama-Yoshida, H. A Density Functional Theory Study of Self-Regenerating Catalysts LaFe1−xMxO3−y (M = Pd, Rh, Pt). *J. Am. Chem. Soc.* **2011**, *133*, 18506−18509.

(36) Gao, Y.; et al. Energetics of Nanoparticle Exsolution from Perovskite Oxides. *J. Phys. Chem. Lett.* **2018**, *9*, 3772−3778.

(37) Gao, Y.; Chen, D.; Saccoccio, M.; Lu, Z.; Ciucci, F. From material design to mechanism study: Nanoscale Ni exsolution on a highly active A-site deficient anode material for solid oxide fuel cells. *Nano Energy* **2016**, *27*, 499−508.

(38) Lv, H.; et al. Situ Investigation of Reversible Exsolution/Dissolution of CoFe Alloy Nanoparticles in a Co-Doped Sr2Fe1.5Mo0.5O6−δ Cathode for CO2 Electrolysis. *Adv. Mater.* **2020**, *32*, 1906193.

(39) Raman, A. S.; Vojvodic, A. Modeling Exsolution of Pt from ATiO3 Perovskites (A = Ca/Sr/Ba) Using First-Principles Methods. *Chem. Mater.* **2020**, *32*, 9642−9649.

(40) Nenning, A.; et al. The Electrochemical Properties of Sr(Ti,Fe)O3-$\delta$for Anodes in Solid Oxide Fuel Cells. *J. Electrochem. Soc.* **2017**, *164*, F364−F371.

(41) Wang, J.; et al. Exsolution Synthesis of Nanocomposite Perovskites with Tunable Electrical and Magnetic Properties. *Adv. Funct. Mater.* **2022**, *32*, 2108005.

(42) Crumlin, E. J.; et al. Surface strontium enrichment on highly active perovskites for oxygen electrocatalysis in solid oxide fuel cells. *Energy Environ. Sci.* **2012**, *5*, 6081−6088.

(43) Bliem, R.; Kim, D.; Wang, J.; Crumlin, E. J.; Yildiz, B. Hf Deposition Stabilizes the Surface Chemistry of Perovskite Manganite Oxide. *J. Phys. Chem. C* **2021**, *125*, 3346−3354.

(44) Jung, W.; Tuller, H. L. Investigation of surface Sr segregation in model thin film solid oxide fuel cell perovskite electrodes. *Energy Environ. Sci.* **2012**, *5*, 5370−5378.

https://doi.org/10.1021/acs.nanolett.2c01439
Nano Lett. 2022, 22, 5401−5408

(45) Momose, Y.; Sakurai, T.; Nakayama, K. Thermal Analysis of Photoelectron Emission (PE) and X-ray Photoelectron Spectroscopy (XPS) Data for Iron Surfaces Scratched in Air, Water, and Liquid Organics. *Applied Sciences* **2020**, *10*, 2111.
(46) Martín-Concepción, A. I.; Yubero, F.; Espinós, J. P.; Tougaard, S. Surface roughness and island formation effects in ARXPS quantification. *Surf. Interface Anal.* **2004**, *36*, 788−792.
(47) Santaya, M.; Toscani, L.; Baqué, L.; Troiani, H. E.; Mogni, L. Study of phase stability of SrTi0.3Fe0.7O3−δ perovskite in reducing atmosphere: Effect of microstructure. *Solid State Ionics* **2019**, *342*, 115064.
(48) Kousi, K.; Neagu, D.; Bekris, L.; Papaioannou, E. I.; Metcalfe, I. S. Endogenous Nanoparticles Strain Perovskite Host Lattice Providing Oxygen Capacity and Driving Oxygen Exchange and CH4 Conversion to Syngas. *Angew. Chem., Int. Ed.* **2020**, *59*, 2510−2519.
(49) Syed, K.; Wang, J.; Yildiz, B.; Bowman, W. J. Bulk and surface exsolution produces a variety of Fe-rich and Fe-depleted ellipsoidal nanostructures in La0.6Sr0.4FeO3 thin films. *Nanoscale* **2022**, *14*, 663−674.
(50) Marrocchelli, D.; Bishop, S. R.; Tuller, H. L.; Yildiz, B. Understanding Chemical Expansion in Non-Stoichiometric Oxides: Ceria and Zirconia Case Studies. *Adv. Funct. Mater.* **2012**, *22*, 1958−1965.

https://doi.org/10.1021/acs.nanolett.2c01439
Nano Lett. 2022, 22, 5401−5408